JACS
JOURNAL OF THE AMERICAN CHEMICAL SOCIETY
Article
pubs.acs.org/JACS

Core-Shell Nanostructured "Black" Rutile Titania as Excellent Catalyst for Hydrogen Production Enhanced by Sulfur Doping

Chongyin Yang,[†,‡] Zhou Wang,[†,‡] Tianquan Lin,[†,‡] Hao Yin,[†] Xujie Lü,[∥] Dongyun Wan,[†] Tao Xu,[§] Chong Zheng,[§] Jianhua Lin,[‡] Fuqiang Huang,*[,†,‡] Xiaoming Xie,[⊥] and Mianheng Jiang[⊥]

[†]CAS Key Laboratory of Materials for Energy Conversion, Shanghai Institute of Ceramics, Chinese Academy of Sciences, Shanghai 200050, P. R. China

[‡]Beijing National Laboratory for Molecular Sciences and State Key Laboratory of Rare Earth Materials Chemistry and Applications, College of Chemistry and Molecular Engineering, Peking University, Beijing 100871, P. R. China

[§]Department of Chemistry and Biochemistry, Northern Illinois University, DeKalb, Illinois 60115, United States

[∥]High Pressure Science and Engineering Center (HiPSEC), University of Nevada, Las Vegas, Nevada 89154, United States

[⊥]State Key Laboratory of Functional Materials for Informatics, Shanghai Institute of Microsystem and Information Technology, Chinese Academy of Sciences, Shanghai 200050, P. R. China

Supporting Information

ABSTRACT: Modification of rutile titanium dioxide (TiO_2) for hydrogen generation and water cleaning is a grand challenge due to the chemical inertness of rutile, while such inertness is a desired merit for its stability in photoelectrochemical applications. Herein, we report an innovative two-step method to prepare a core−shell nanostructured S-doped rutile TiO_2 (R′-TiO_2-S). This modified black rutile TiO_2 sample exhibits remarkably enhanced absorption in visible and near-infrared regions and efficient charge separation and transport. As a result, the unique sulfide surface (TiO_{2-x}:S) boosts the photocatalytic water cleaning and water splitting with a steady solar hydrogen production rate of 0.258 mmol h^{-1} g^{-1}. The black titania is also an excellent photoelectrochemical electrode exhibiting a high solar-to-hydrogen conversion efficiency of 1.67%. The sulfided surface shell is proved to be an effective strategy for enhancing solar light absorption and photoelectric conversion.

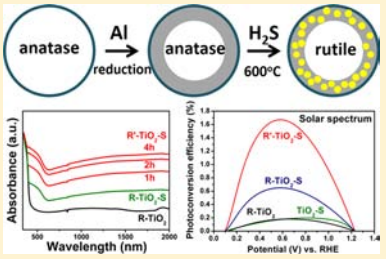

INTRODUCTION

Anatase titania (TiO_2) as a promising solar-driven photocatalyst has attracted enormous attention for hydrogen generation and water cleaning.[1−3] Rutile is another important allotrope of TiO_2 with a narrower band gap (3.0 eV) than anatase (3.2 eV) but has much less photocatalytic activity.[4] Much effort has been made on anatase to improve its ultraviolet (UV) and visible-light photocatalytic capability by controlling its microstructure (morphology, size, crystallinity, and facets) and by tuning its band structure near the valence maximum and conduction band minimum (with element doping, oxygen vacancies, etc.).[5−10] These strategies may also work for rutile TiO_2 to capture energies in the UV region, which is about only 5% of the incoming solar spectrum. Therefore, an efficient strategy to enhance the photoactivity of rutile is to extend its light absorption capability into the visible region.[11] Wide−band gap anatase TiO_2 was reported to have better solar absorption and photocatalytic activity with the doping of nonmetal ions such as S^{2-}.[12−14] There were also similar S-doping investigations on rutile TiO_2, but the doping level is too low to achieve a significant improvement.[15−18] Hence, the current photocatalytic activity of rutile TiO_2 remains insufficient.

The recent research and developments on black titania have led to a brand new direction in photocatalysis and photoelectrochemical material modification.[19−21] Herein, we report a two-step strategy for enhancing both UV and visible-light photocatalysis and photoelectrochemical (PEC) water splitting using our synthesized S-doped black rutile titania. Unlike the traditional reduced TiO_2 with highly unstable surface oxygen defects in air,[22] the "black" TiO_2 reported in this work has disordered surface layers with a large amount of stable Ti^{3+} and oxygen vacancy (V_O) dopants introduced during the initial formation process. These features enable visible and infrared light absorption of the material. Next, these disordered TiO_{2-x} surface layers become accessible to sulfur anions S^{2-}, which further enhance the visible-light absorption. In contrast, due to the closer lattice packing of rutile TiO_2 that limits the access of gas molecules, 'black' rutile TiO_2 cannot be produced via the reported hydrogen reduction method, although black anatase TiO_2 is attainable by reducing anatase in high pressure H_2 over several days.

In this study, a transformative two-step approach is conducted to prepare a core−shell nanostructure of 'black' rutile TiO_2 with sulfided surface (TiO_{2-x}:S). The black TiO_{2-x} with disordered surface is obtained by reducing TiO_2 with molten aluminum (Al) in a two-zone furnace.[23] This two-step process of S-doped rutile TiO_2 can be readily achieved using

Received: July 25, 2013
Published: October 28, 2013

dx.doi.org/10.1021/ja4076748 | J. Am. Chem. Soc. 2013, 135, 17831−17838

either rutile or anatase TiO_2 as raw material, and the final product is consistently to be rutile. This is because there is enough activation energy at 600 °C in a flow of H_2S for the phase transition from anatase to rutile to occur. The unique 'black' surface layer in our Al-reduced black rutile TiO_2 exhibits drastically enhanced light absorption in visible and near-infrared regions that leads to nearly 30-fold improvement over pristine rutile TiO_2 in photocatalytic water-splitting activity. The loosely packed microstructure ensures a high concentration of S^{2-} anions (>4.68 at. %) to be intercalated into the disordered shell of rutile TiO_2. These S^{2-} anions subsequently occupy the oxygen vacancies, further narrowing the band gap by introducing new electronic transitions from the S 3p orbitals to the Ti 3d orbitals. Consequently, absorption of the S-doped TiO_2 extends into visible and infrared regions. Our work demonstrates that this simple two-step approach can significantly enhance the photoconversion efficiency of rutile TiO_2 by introducing an Al-reduced 'black' surface stabilized with S-doping.

EXPERIMENTAL SECTION

Preparation of R-TiO_2-S and R′-TiO_2-S. Both commercial rutile and anatase TiO_2 were employed as starting materials to prepare surface-modified rutile TiO_2 nanoparticles, as illustrated in Figure 1a,b. The materials have average particle sizes of ∼30 nm in diameter. They were first reduced by molten Al to form a disordered TiO_{2-x} shell. (The Al-reduced rutile and anatase samples are denoted as R-TiO_{2-x} and A-TiO_{2-x}, respectively.) The Al powders and pristine TiO_2 were separately placed in an evacuated two-zone furnace of 800 °C (molten Al) and 500 °C (TiO_2) for 6 h in a 5×10^{-4} Pa pressure (Figure S1). Then, the as-reduced samples were heated at 600 °C for 4 h in a 1000 Pa H_2S atmosphere to dope sulfur into the oxygen-deficient shell of titania. (The sulfided rutile and anatase samples are denoted as R-TiO_2-S and R′-TiO_2-S, respectively.) The same commercial rutile was directly annealed under the same H_2S-atmosphere condition as a reference sample (TiO_2-S).

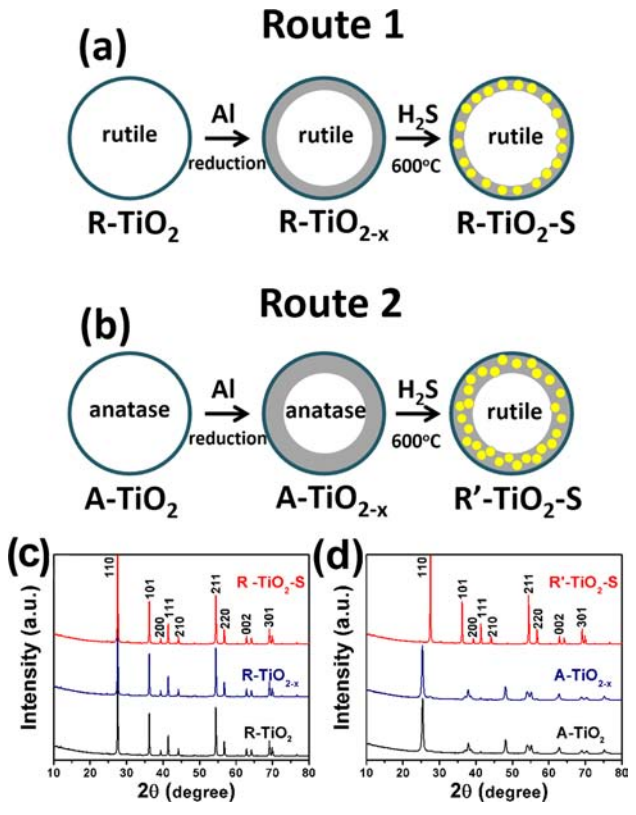

Figure 1. (a,b) Two schematic synthetic routes of rutile TiO_2 with sulfided surface. The shaded area is the disordered layer and white region the crystalline core. (c,d) XRD patterns of as-prepared R-TiO_2-S, R-TiO_{2-x}, pristine R-TiO_2, and R′-TiO_2-S, A-TiO_{2-x}, and pristine A-TiO_2.

Preparation of R-TiO_2-S and R′-TiO_2-S Films. R′-TiO_2-S, R-TiO_2-S, TiO_2-S, and R-TiO_2 films were prepared by a spin-coating method. The R-TiO_2 and A-TiO_2 powders were dispersed in ethanol and then milled for 6 h to obtain a slurry. The precursor thin films of the two samples were spin-coated on FTO substrates with the slurry. The precursor films were further treated by Routes 1 and 2 in the same procedure as the powder samples.

Photocatalytic Methyl Orange Decomposition. The photocatalytic activities of the samples were evaluated by monitoring the decomposition of methyl orange (MO) in an aqueous solution. After stirring for 30 min in dark, the solution was illuminated with a 300 W Hg lamp or an AM 1.5 simulated solar light source. The photocatalysis reaction was carried out at pH = 7.0.

Photocatalytic H_2 Generation. 100 mg photocatalyst loaded with 0.5 wt % Pt was placed into an aqueous methanol solution (120 mL, 25%) in a closed gas circulation system. An AM 1.5 simulated solar power system was used as light irradiation source. Methanol was used as a sacrificial reagent, therefore the anodic reaction generating O_2 from H_2O did not occur. The amount of H_2 generated was determined by gas chromatography.

Photoelectrochemical Cell (PEC). PEC measurements were performed in a typical three-electrode electrochemical workstation (CHI600B) in which the TiO_2 film on FTO substrate, a Pt wire, and an Ag/AgCl electrode were used as the working, counter, and reference electrodes, respectively. A 1.0 M NaOH aqueous solution was used as the supporting electrolyte to maintain the stability of the film. A solar simulator (AM 1.5) with a power of 100 mW/cm^2 was used as the illumination source. Photocurrent with ON/OFF cycles was measured using the same electrochemical workstation coupled with a mechanical chopper.

RESULTS AND DISCUSSION

Both Routes 1 and 2 were employed to prepare surface-modified rutile TiO_2 nanoparticles. Two raw materials, rutile and anatase, were first reduced by molten Al to form a disordered TiO_{2-x} shell. H_2S atmosphere was employed to dope sulfur into the oxygen-deficient shell of titania. The X-ray diffraction (XRD) patterns of all samples prepared via Route 1 were indexed in accordance with the rutile structure, as shown in Figure 1c,d. Both the pristine A-TiO_2 and Al-reduced A-TiO_{2-x} samples prepared via Route 2 exhibit typical anatase patterns, while the R′-TiO_{2-x}-S sample shows a pure rutile phase corresponding to the ICSD card of rutile TiO_2 (PDF no. 87-0920).[24] As H_2S reduces the activation energy for atatase-to-rutile phase transition, the anatase phase can readily transform to the rutile allotrope.[25] The structural change was also examined by monitoring the Raman spectrum (Figure S2) during the phase transition. For pristine A-TiO_2 and A-TiO_{2-x}, six Raman active modes ($3E_g + 2B_{1g} + A_{1g}$) with frequencies at 144, 197, 399, 515, 519 (superimposed with the 515 cm^{-1} band), and 639 cm^{-1} are indexed as from the anatase phase.[3] The shift and broadening of the A-TiO_{2-x} Raman peaks indicate that the original symmetry of TiO_2 lattice is reduced due to the surface disorder after the Al-reduction process. The R′-TiO_{2-x}-S exhibits characteristic Raman modes of rutile TiO_2 at 146 cm^{-1} (B_{1g}), 443 cm^{-1} (E_g), and 609 cm^{-1} (A_{1g}). The mode at 243 cm^{-1} (E_g) is also a multiphonon peak characteristic of rutile.[26]

dx.doi.org/10.1021/ja4076748 | J. Am. Chem. Soc. 2013, 135, 17831−17838

High-resolution transmission electron microscopy (HRTEM) images of R-TiO_{2-x}, R-TiO_2-S, A-TiO_{2-x}, and R′-TiO_2-S are shown in Figure 2. In both routes, the Al-reduced

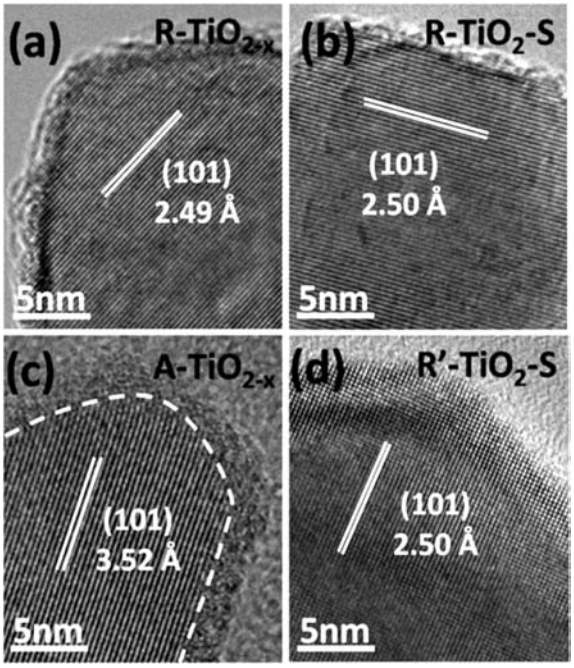

Figure 2. HRTEM images of (a) R-TiO_{2-x}, (b) R-TiO_2-S, (c) A-TiO_{2-x}, and (d) R′-TiO_2-S. The dash line is the interface of the disordered layer and crystalline core.

samples display a core−shell structure consisting of a crystalline core of TiO_2 with a disordered shell layer (TiO_{2-x}). The crystalline core of R-TiO_{2-x} and A-TiO_{2-x} shows well-resolved (101) lattice planes with typical rutile and anatase *d*-spacing of 2.49 and 3.52 Å, respectively (Figure 2a,c). The disordered surface layer in R-TiO_{2-x} is only a few atomic layer thick. Remarkably, the A-TiO_{2-x} sample shows a much thicker (∼2 nm thick) disordered surface layer. We also found that anatase is easier to be reduced by Al than rutile. Figure 2b shows that the R-TiO_2-S nanoparticles synthesized via Route 1 retain the microstructure composed of a crystalline core and an amorphous shell after sulfidation. As a reference, the HRTEM image of TiO_2-S shows no obvious structure rearrangement near the surface region (Figure S3). The nanocrystals of R′-TiO_2-S from Route 2 show a well-resolved (101) lattice plane with a *d*-spacing of 2.50 Å without any obviously disordered shell. The entire core of all starting nanoparticles has transformed into the rutile phase, as demonstrated by the XRD results. Furthermore, the disordered surface layer formed by the Al-reduction process has recrystallized during the phase transition (Figure 2d), and the doped S^{2-} and stabilized Ti^{3+} atoms are mainly localized near the surface. Obviously, Route 2 is more efficient than Route 1 in terms of reorganizing the surface of rutile TiO_2. The elemental mapping (Figure S4) of R′-TiO_2-S confirms that the S-dopants are located on the surface layer. The bulk concentration of S was investigated by quantitative analyses of energy-dispersive X-ray spectroscopy (EDS) are 0.87 at. % and 2.72 at. % for R-TiO_2-S and R′-TiO_2-S samples, respectively. The EDS measurements are summarized in Table S1.

The sulfided surface strongly enhances the solar light absorption as evidenced by Figure 3a which displays the diffuse

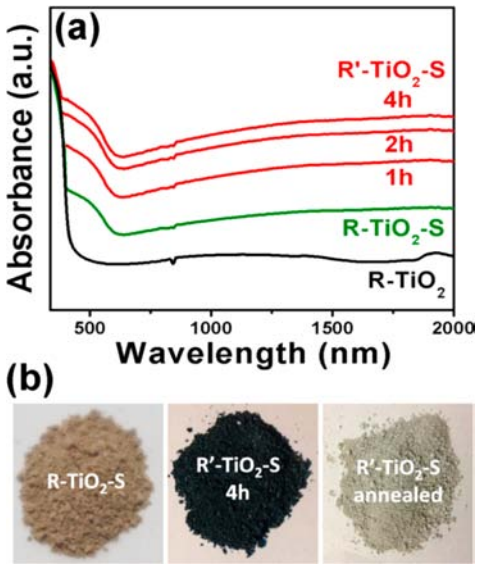

Figure 3. (a) Diffuse reflectance spectrum of R-TiO_2, R-TiO_2-S, and R′-TiO_2-S with different sulfidation time. (b) Photographs of as-prepared R-TiO_2-S, R′-TiO_2-S-4h, and R′-TiO_2-S annealed at 800 °C in Ar atmosphere.

reflectance spectra of as-prepared R-TiO_2-S and R′-TiO_2-S. The commercial R-TiO_2 is used as a reference. The absorption edges near 400 nm from the core of crystalline rutile TiO_2 corresponds to its intrinsic band gap (3.0 eV). A secondary absorption region was observed from 3.0 to 1.7 eV, which is attributed to the S-doping effect. Compared with the directly sulfided rutile TiO_2 (Figure S6), all our samples show significantly enhanced absorptions in the region between 400 and 2000 nm, covering both visible and near-infrared (NIR) regions, while the black sample R′-TiO_2-S-4h exhibits the highest absorption, much greater than the light brown sample of R-TiO_2-S (Figure 3b). We attribute the above observation to the fact that R′-TiO_2-S has thicker sulfided surface layer than that R-TiO_2-S, because its starting material, i.e., anatase TiO_2 is more prone to the reduction by Al than rutile. Furthermore, the absorption enhancement for all R′-TiO_2-S samples is highly dependent on the Ti^{3+} and S^{2-} doping levels that are proportional to the sulfidation time. It can be seen in Figure 3a that the absorption increases with sulfidation time ranging from 1 to 4 hours. At 4 hours, sulfidation reaches saturation since longer sulfidation does not lead to higher absorption. All results indicate that the incorporation of Ti^{3+} and S^{2-} dopants successfully extends the light absorption from the UV into the visible and NIR region, resulting in wider spectrum solar absorption in rutile TiO_2. The comparison of the absorption spectra of A-TiO_{2-x} and R′-TiO_2-S is shown in Figure S7. It demonstrates that the enhanced absorption spectrum, especially in the NIR region, should result from oxygen deficiencies that are directly related to the presence of Ti^{3+}. This enhanced wide-spectrum absorption is also related to the high electron concentration introduced by oxygen vacancies (V_O) in the surface layer, as similar phenomenon has been observed in transparent conducting oxide (TCO) films.[27] In order to verify this hypothesis, polycrystalline rutile TiO_2 thin film samples (200 nm thick) were prepared by magnetron sputtering and further treated according to Routes 1 and 2, respectively. The SEM image of the cross-section is shown in Figure S8. The Hall measurement shows that the square

dx.doi.org/10.1021/ja4076748 | J. Am. Chem. Soc. 2013, 135, 17831−17838

resistances of the black disks (R-TiO_2-S and R′-TiO_2-S) are as low as 3961 Ω/sq (electron concentration: 6.21×10^{18} cm^{-3}) and 997 Ω/sq (electron concentration: 4.92×10^{19} cm^{-3}), respectively. These measured electron concentrations might be lower than the actual value of the S-doped 'black' surface layer because the measurement is the averaged value of both surface layer and bulk. In addition, the intense secondary absorption edge is due to an upward shift of the valence band maximum (VBM) by S doping. The existence of S^{2-} and Ti^{3+}-rich surface layer can be indirectly probed by the comparison of the 4h R′-TiO_2-S sample before and after further annealing in Ar. Upon annealing in Ar at 800 °C for 30 min, the 4h R′-TiO_2-S sample turned to light gray. We believe that such a color change is caused by the diffusion of S^{2-} and Ti^{3+} atoms from surface to bulk, i.e., the dilution of the "color centers".

From the DFT calculated total and projected partial DOS (Figure S9), we found that the primary effect of S-doping in TiO_2 nanocrystals is to produce strong tailing near the valence band (VB) edge. The tailing effect leads a remarkable band gap narrowing (to ∼0.6 eV). Furthermore, surface defects and reconstruction introduce localized states of Ti^{3+} $3d^1$ below the CB minimum of black TiO_{2-x}:S. Therefore, the electronic transitions from the tailed VB to the tailed CB are responsible for the vis-NIR absorption in our black rutile samples.

The VB and S 2p X-ray photoemission spectrum (XPS) are shown in Figure 4. The complete XPS spectra of R′-TiO_2-S

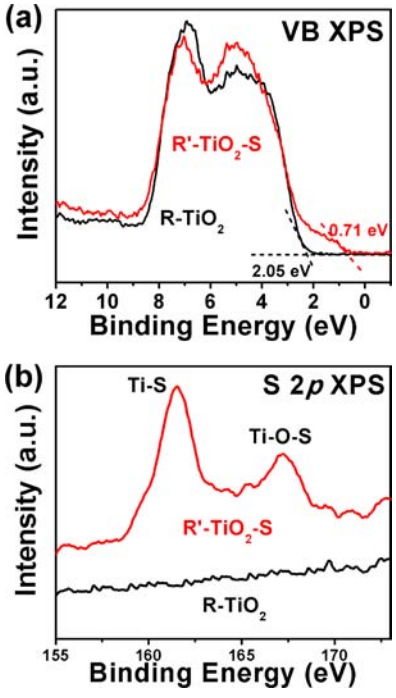

Figure 4. (a) VB and (b) S 2p XPS spectrum of R′-TiO_2-S and R-TiO_2.

sample are shown in Figure S10a. The R-TiO_2 displays a typical VB DOS characteristic of TiO_2, with the edge of the maximum energy at about 2.05 eV.[7] For R′-TiO_2-S, the VBM moves toward the vacuum level at ∼0.71 eV. Two broadened peaks of S 2p were observed at 161.6 and 167.4 eV in R′-TiO_2-S, as shown in Figure 4b. The peak at 161.6 eV is from the S atoms at the oxygen defects, as it is close to the binding energy in TiS_2 (161.7 eV).[28] The peak at 167.4 eV is attributed to the S atoms in mixed Ti-O-S bonding environment.[29] The S-doping levels in R-TiO_2-S and R′-TiO_2-S determined by XPS are 1.35 at. % and 4.68 at. %, respectively. Also, XPS spectra show no signal of Al element (Figure S10b).

The presence of Ti^{3+} in the as-prepared samples was investigated by electron paramagnetic resonance (EPR). The EPR spectrum of A-TiO_{2-x} and R′-TiO_2-S show intense signals centered on the *g*-value of 2.02 (Figure 5a). The paramagnetic

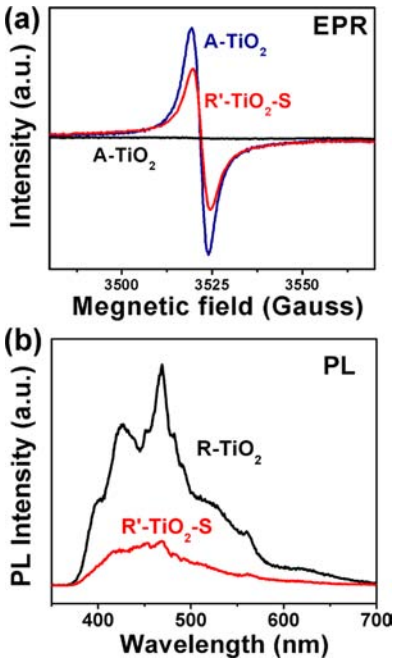

Figure 5. (a) EPR spectrum of of R′-TiO_2-S, A-TiO_{2-x}, and pristine A-TiO_2. (b) Photoluminescent spectrum of R′-TiO_2-S and R-TiO_2.

signal peaks are assigned to the large amount of O_2^- adsorption due to the Ti^{3+} existing in the surface layer.[30] The concentration of Ti^{3+} was determined by a numerical double integration of the EPR spectra in comparison with a frozen aqueous solution of Cu^{2+}. The concentration of O_2^- was estimated to be 260 μmol cm^{-3}. As expected, the signal intensity of EPR decreases significantly after sulfidation due to the decrease of the Ti^{3+} concentration of caused by S^{2-} substitution.

We also measured the photoluminescence (PL) emission of the samples in order to understand the behavior of light-generated electrons and holes in our samples since PL emission is a result of the recombination of the free carriers.[31] The PL spectra of pristine and hydrogenated TiO_2 samples in the wavelength range of 350−700 nm with the excitation light at 320 nm are shown in Figure 5b. The shapes of the emission spectra of different samples are similar. Three main emission peaks are observed at 410 nm (3.0 eV), 423 nm (2.9 eV), and 464 nm (2.7 eV), respectively. The first one is attributed to the emission of band gap transition of rutile. The peaks at 450 and 468 nm are attributed to the free excitons at the band edge. The remaining two peaks at 482 and 492 nm are assigned to the bound excitons.[32] In addition, several small PL peaks observed in the wavelength range are mainly due to the surface defects of the TiO_2 samples. The PL peak intensity of the R′-TiO_2-S sample is much lower than that of R-TiO_2. This observation indicates that the R′-TiO_2-S sample has a relatively low recombination rate of electrons and holes, which normally favors high photocatalytic activity.

dx.doi.org/10.1021/ja4076748 | J. Am. Chem. Soc. 2013, 135, 17831−17838

The as-prepared rutile TiO_2 samples with sulfided surface are expected to exhibit considerable photocatalysis enhancement in comparison to pure rutile TiO_2 (R-TiO_2). Next, MO was used as a probe to investigate the photocatalytic performance of the prepared samples, and R-TiO_2 was used as a reference sample. The specific surface areas of the R′-TiO_2-S (~44 m^2/g), R-TiO_2-S (~42 m^2/g), and R-TiO_2 (~43 m^2/g) are similar. Therefore the photocatalytic difference of the samples should not come from the surface area variation. Photodegration of the same MO solution under UV-light irradiation was completed in 45 min for R′-TiO_2-S, while during the same period only 59% and 49% of MO were photodegraded by R-TiO_2-S and R-TiO_2 (Figure S11a). This experiment indicates that R′-TiO_2-S exhibits much higher UV-light photocatalytic activity than R-TiO_2 and R-TiO_2-S. The MO decomposition rate of R′-TiO_2-S increases with the S-doping level in the surface layer, as shown in Figure S11b. Apparently, the S-doping is the key factor for enhancing photocatalytic activity. Similarly, visible-light photocatalytic decomposition experiments of MO were conducted using a 420 nm cutoff filter, the results being shown in Figure 6a. Again, the S incorporation greatly boosted their visible-light photocatalytic capability. The R′-TiO_2-S completely decomposed MO in 4 h, while R-TiO_2-S degraded only ~22% and R-TiO_2 almost none. Compared with the directly sulfided rutile TiO_2 (Figure S12), the rutile TiO_2 samples prepared via our two-step sulfidation process show much higher Ti^{3+} and S^{2-} concentrations, leading to the observed superior photocatalytic activity.

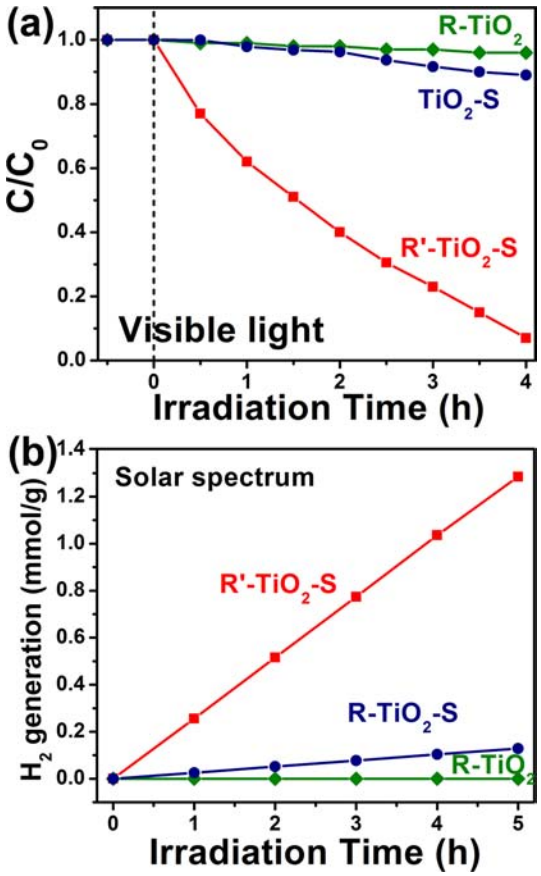

Figure 6. Visible-light driven photocatalytic (a) decomposition of MO and (b) water splitting for H_2 generation by R′-TiO_2-S, R-TiO_2-S, and R-TiO_2.

The photocatalytic activities of the samples for water splitting were also measured. Figure 6b shows the time evolution of H_2 for as-prepared samples. Apparently, the reactions are all zeroth order, which is typical for heterogeneous photochemical reactions where the reaction rate is independent of the mass flow of the reactants, because the reactants saturate the surface catalytic sites of the photocatalysts. Therefore, the reaction rate depends only on the nature of the catalyst and the photon flux. Under the above reaction conditions, the sample could steadily produce hydrogen at about 0.258 μmol h^{-1} g^{-1}, which is a much higher rate than that of the reaction catalyzed by other rutile TiO_2 (<100 μmol h^{-1} g^{-1}).[33] No noticeable decrease in H_2 production rate in five cycling tests was observed within the 20 h photocatalytic period (Figure S13). Under the same photoreaction condition, R′-TiO_2-S exhibits a nearly 10-fold improvement over R-TiO_2-S (258 vs 29 μmol h^{-1} g^{-1}). Considering that pure rutile TiO_2 can barely produce H_2, the photocatalytic capability of our core−shell structured R′-TiO_2-S is fairly striking.

In order to further investigate the photoelectrochemical properties, R′-TiO_2-S, R-TiO_2-S, TiO_2-S, and R-TiO_2 films were prepared by a spin-coating method. The photocurrents of these films were recorded in dark and under illumination from an AM 1.5 solar spectrum simulator with a set of chopped linear-sweeps, as shown in Figure 7a. The potential was swept linearly at a scan rate of 10 mV/s between 0.0 and 1.5 V_{RHE} in 1 M NaOH eletrolyte (pH = 13.6). Both photoelectrodes showed insignificant dark current (<10^{-4} mA/cm^2) indicating that no

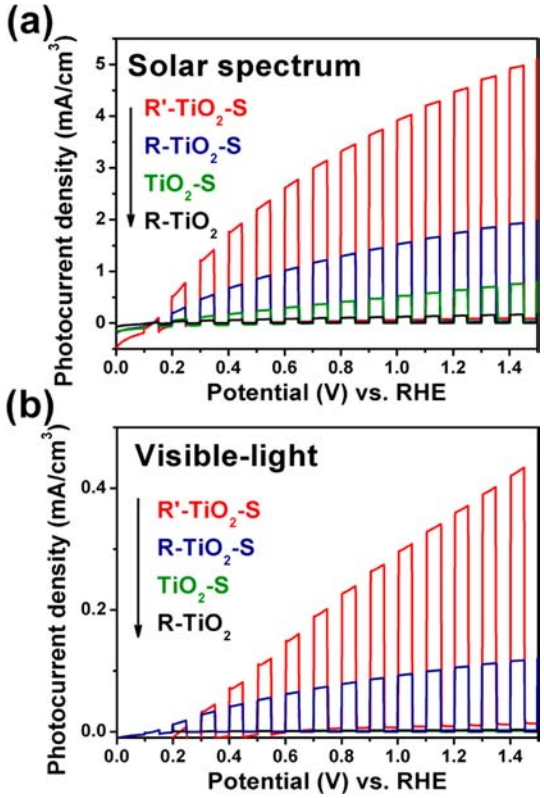

Figure 7. Photoelectrochemical properties of R′-TiO_2-S, R-TiO_2-S, TiO_2-S, and R-TiO_2 electrodes: Chopped $J-V$ curves under (a) simulated solar light illumination and (b) visible-light illumination using a three-electrode setup (TiO_2 working, Pt counter, Ag/AgCl reference electrode, scan rate of 10 mV/s) in 1 M NaOH electrolyte (pH = 13.6).

dx.doi.org/10.1021/ja4076748 | J. Am. Chem. Soc. 2013, 135, 17831−17838

electrocatalytic oxygen evolution occurred. Under solar light illumination, the R′-TiO_2-S and R-TiO_2-S electrodes demonstrated 30- and 11-fold increase of photocurrent density, respectively, compared to R-TiO_2 at 1.23 V_{RHE} (corresponding to the potential of the reversible hydrogen electrode). Furthermore, the onset potential of photocurrent revealed a drastic shift from 0.41 V_{RHE} for R-TiO_2 to 0.13 V_{RHE} for R′-TiO_2-S. The improvement of photocurrent densities was also shown in the chopped linear sweeps under solar illumination with a 420 nm optical high-pass filter (Figure 7b). The higher photocurrent density, the lower onset potential and extended photoresponse range of the "black" TiO_{2-x} is an indication of more efficient charge separation and transport in the sample.

The solar-to-hydrogen (STH) efficiencies (η) of photoanodes can be calculated using the equation[36]

$$\eta = I(1.23 - V)/J_{light}$$

where V is the applied bias vs RHE, I is the photocurrent density at the measured bias, and J_{light} is the irradiance intensity of 100 mW/cm^2 (AM 1.5G). The calculated STH efficiency plotted as a function of the applied bias is shown in Figure 8a.

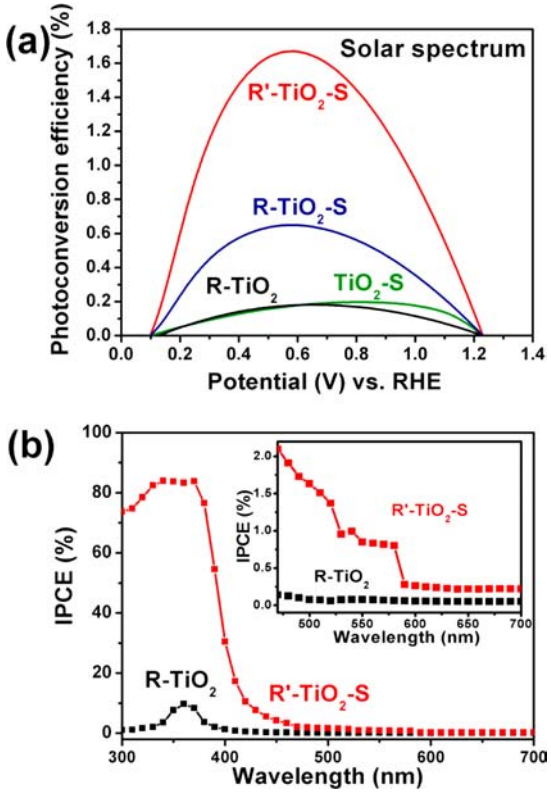

Figure 8. Photoelectrochemical properties of R′-TiO_2-S, R-TiO_2-S, TiO_2-S and R-TiO_2 electrodes: (a) photoconversion efficiency as a function of applied potential; (b) IPCE spectra in the region of 300−700 nm at 0.65 V_{RHE}; Inset: IPCE spectra in the region of 420−700 nm.

The R-TiO_2 and TiO_2-S samples show conversion efficiencies of ∼0.18% at 0.65 V_{RHE} and ∼0.20% at 0.77 V_{RHE}. The R′-TiO_2-S and R-TiO_2-S samples achieved excellent efficiencies of ∼1.67% and ∼0.65% at a lower bias of 0.57 V_{RHE}, which is among the best STH efficiencies (0.5% ∼ 1.6%) for TiO_2-based photoanodes.[34,35]

In order to investigate the extended visible-light absorption of the "black" TiO_2, we also measured the incident photon-to-current conversion efficiency (IPCE) for R-TiO_2 and R′-TiO_2-S photoanodes at 0.65 V_{RHE} (Figure 8b). The IPCE can be expressed by the equation of[36]

$$\text{IPCE} = (1240I)/(\lambda J_{light})$$

where I is the measured photocurrent density at a specific wavelength, λ is the wavelength of incident light, and J_{light} is the measured irradiance at a specific wavelength. Comparing with R-TiO_2, R′-TiO_2-S exhibits greatly enhanced IPCE value in the entire UV region, reaching 74.3% ∼ 84.0% in the wavelength range from 300 to 380 nm. Moreover, the IPCE value was even larger in the visible-light region from 400 to 580 nm for the R′-TiO_2-S sample, in agreement with the extended absorption in the diffuse reflectance seperiment (Figure 3a). The enhancement of the IPCE value shows that that the Al-reduced sulfided surface also extends effectively the photoresponse range into the visible-light.

The electrochemical impedance measurements of R′-TiO_2-S, R-TiO_2-S, and R-TiO_2 samples showed positive slopes in the Mott-Schottky plots, indicating the n-type semiconductor behavior (Figure 9). The R′-TiO_2-S and R-TiO_2-S samples

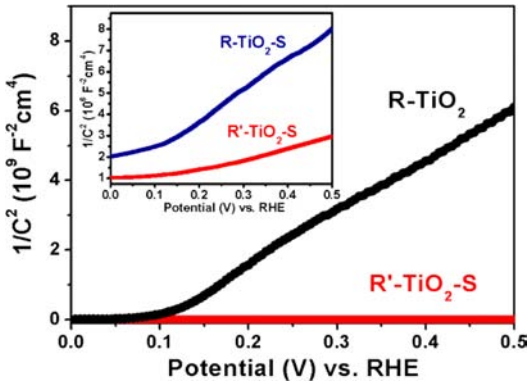

Figure 9. Mott−Schottky plots of R′-TiO_2-S, R-TiO_2-S, and R-TiO_2 electrodes collected at a frequency of 5 kHz in dark.

showed smaller slope in the Mott−Schottky plot than the R-TiO_2 sample, implying a much higher free charge carrier density. The carrier density can be calculated from the slope of Mott−Schottky plots using the following equation[36]

$$N_c = (2/e_0\varepsilon\varepsilon_0)[\mathrm{d}(1/C^2)/\mathrm{d}V]^{-1}$$

where e_0 is the electron charge, ε the dielectric constant of TiO_2 (ε = 170), ε_0 is the permittivity of vacuum, N_c is the carrier density, and V is the applied bias. The calculated electron using the equation densities of the R′-TiO_2-S, R-TiO_2-S, and R-TiO_2 are 3.92×10^{20}, 1.09×10^{19} and 6.17×10^{17} cm^{-3}, respectively, in accordance with the Hall measurements. High electron density indicates large upward shift of the Fermi level in the shell of our S-doped black TiO_2. This shift can lead a significant bending of the band edge, which facilitates charge separation at the shell layer and electrolyte interface. It also explains why the core−shell nanostructure with sulfided surface (TiO_{2-x}:S) can boost hydrogen production of rutile TiO_2.

To evaluate the stability of the S-doped black rutile TiO_2, the long-term photoelectrochemical stability of R′-TiO_2-S electrode was measured under illumination for 30 h in the electrolytes with different pH values. The plots of current vs time (Figure

dx.doi.org/10.1021/ja4076748 | J. Am. Chem. Soc. 2013, 135, 17831−17838

10a) were collected in 1 M KOH/KH_2PO_4/K_2HPO_4/H_3PO_4 electrolytes at pH = 1, 4, 7, 10, and 13, respectively. The

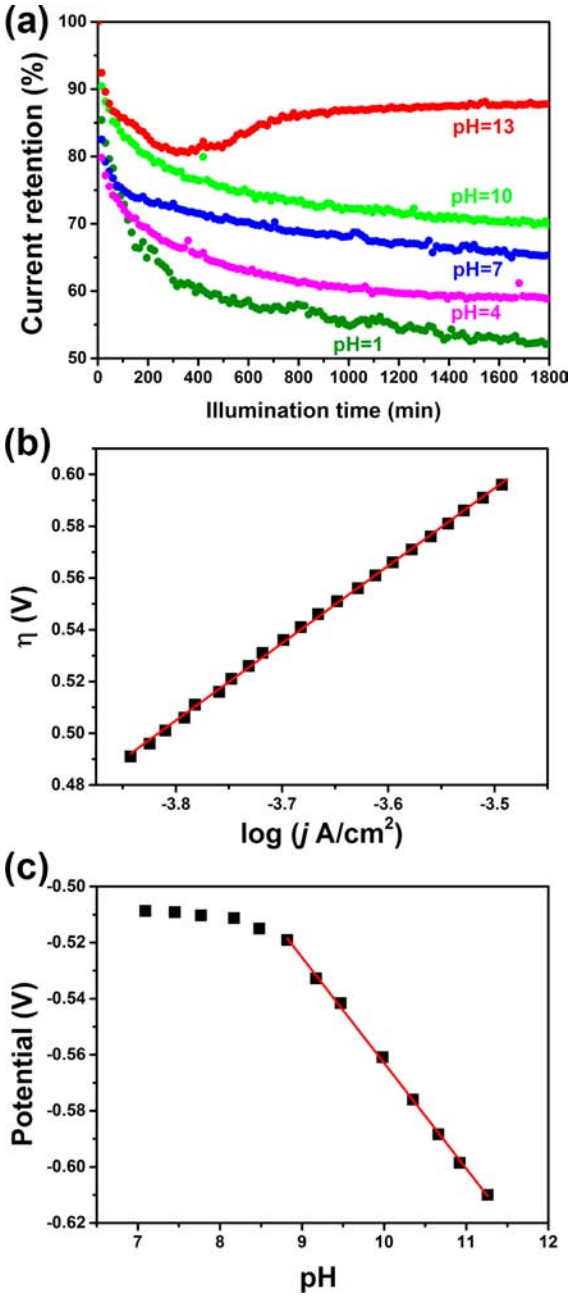

Figure 10. (a) The plots of current vs time of R′-TiO_2-S electrode in in the electrolytes with different pH values. (b) Tafel plots (E vs log(j)), $\eta = (E - E_0)$, for R′-TiO_2-S film operated in 1 M NaOH electrolyte. Tafel slope is 29.9 mV/decade. (c) The pH dependence of steady-state electrode potential at constant current density (j = 10 μA cm^{-2}) operated in 1 M KOH/KH_2PO_4/K_2HPO_4 electrolyte. Slope is −36.4 mV/pH unit.

potential of the reversible hydrogen electrode (V_{RHE}) can be calculated using the equation

$$V_{RHE} = V_{Ag/AgCl} + 0.059pH + 0.1976$$

In order to obtain the same photoelectrochemical reaction kinetics, 0, 0.18, 0.36, 0.54, 0.72 $V_{Ag/AgCl}$ were applied at pH = 13, 10, 7, 4, and 1 to set the same 1.0 V_{RHE}. The photoelectrochemical currents at different pH values all decrease relatively rapidly in the initial 3 h and then tend to be stable. After 30 h, the current retentions are 52% at pH = 1, 59% at pH = 4, 65% at pH = 7, and 70% at pH = 10, respectively. Surprisingly, at pH = 13, the current decreases to the lowest value of 80% and then increases to a stable value of 88%. Apparently, the S-doped black rutile TiO_2 shows better long-term photoelectrochemical stability in alkaline electrolyte than in acidic electrolyte, most likely because the S dopant is relatively unstable in a low pH environment.

Furthermore, we investigated in more details of the operational redox reaction using the standard electrochemical kinetic approach.[37] The simplest reactions that can account for the redox conversions on photoelectrochemical electrodes are the following:

$$H_2O + 2h^+ \rightarrow 1/2O_2 + 2H^+ (\text{on the surface of R′-}TiO_2\text{-S electrode})$$

$$2H^+ + 2e^- \rightarrow H_2 (\text{on the surface of Pt electrode})$$

Therefore, we studied the dependence of R′-TiO_2-S electrode potential on current density and pH, under illumination at room temperature. The data presented in Figure 10 provide a direct confirmation of the following electrochemical rate law which is consistent with the reactions of water splitting,

$$j = k_o a(H^+)^{-x} \exp\left(-\frac{FE}{nRT}\right)$$

here j is the current density, k_o is a potential-independent constant, a(H^+) is the activity of alkali-metal cation or proton (proportional to the ion/proton concentration in the dilute limit), E is the electrode potential, F is the Faraday constant, R is ideal gas constant, and T is temperature. The steady-state current density (j) for oxygen evolution from R′-TiO_2-S electrode was evaluated as a function of the overpotential (η) in stirred solutions of 1 M NaOH (pH = 13.6) electrolyte (Figure 10b). The applied voltage (E) was varied in 5 mV increments in the region of water oxidation and maintained until j attained a steady-state value. The corrected potential (E) was converted to η by subtraction of the thermodynamic potential for water oxidation (E_0) under the experimental conditions. Specifically, the slope in the first Tafel plot (Figure 10b), $\partial E/\partial \log(j)$, is 29.9 mV/decade, which is very close to the 29.6 mV/decade value that corresponds to 2.3 × RT/2F. This result strongly supports an n = 2 reaction as electrons, and holes should be in this case for photoelectrochemical water splitting.[38] To evaluate the reaction order in H^+ activity, galvanostatic steady-state potentials of the R′-TiO_2-S electrode were collected as a function of pH at 10 μA cm^{-2}. The plot of potential as a function of pH (Figure 10c) shows a limiting slope (pH > 9) of −36.4 mV/decade that corresponds to x = 1.23. The bifurcation observed at pH = 9 may indicate that there is a change in mechanism (such as a change in Tafel slope) at pH = 9. The two Tafel slopes as well as the inverse first-order rate dependence on H^+ activity establish R′-TiO_2-S as an ideal photocatalyst for water splitting.

■ CONCLUSIONS

We have developed a simple two-step approach for the production of core−shell structured rutile TiO_2 nanoparticles with sulfided shell (TiO_{2-x}:S) and rutile core. The process

dx.doi.org/10.1021/ja4076748 | J. Am. Chem. Soc. 2013, 135, 17831−17838

consists of reduction by molten Al, and the following sufidation in H_2S. The significantly improved photocatalytic activity of the engineered samples is attributed to the high Ti^{3+} and S doping level in the shell layer which extends the light absorption from the UV region into the visible and NIR region. The R′-TiO_2-S (4 h) sample exhibits much greater photocatalytic activity than pure rutile TiO_2 as evidenced by the steady and abundant solar hydrogen production at a rate of 0.258 μmol h^{-1} g^{-1}. The "black" titania is also an excellent photoelectrochemical electrode exhibiting a high solar-to-hydrogen efficiency of 1.67%. In perspective, the simple treatment of pristine TiO_2 by the reduction in melted Al and sulfidation in H_2S provides a scalable and cost-effective synthetic approach to produce efficient photocatalysts for technological implementation of solar hydrogen production and solar water purification.

■ ASSOCIATED CONTENT

Ⓢ Supporting Information

Detail sample characterizations, XRD, XPS, Raman, TEM, and cycling tests of photocatalytic. This material is available free of charge via the Internet at http://pubs.acs.org.

■ AUTHOR INFORMATION

Corresponding Author

huangfq@mail.sic.ac.cn

Notes

The authors declare no competing financial interest.

■ ACKNOWLEDGMENTS

This work is financially supported by NSF of China (grant nos. 51125006, 91122034, 51121064, 61376056), 863 Programs of China (grant no. 2011AA050505), CAS program (grant nos. KJCX2-EW-W11, KGZD-EW-303), and STC of Shanghai (grant no.13JC1405700). T.X. acknowledges the support from the U.S. National Science Foundation (CBET-1150617).

■ REFERENCES

(1) Gratzel, M. *Nature* **2001**, *414*, 338.
(2) Hoffmann, M. R.; Martin, S. T.; Choi, W.; Bahnemann, D. W. *Chem. Rev.* **1995**, *95*, 69−96.
(3) Chen, X.; Mao, S. S. *Chem. Rev.* **2007**, *107*, 2891−2959.
(4) Linsebigler, A. L.; Lu, G.; Yates, J. T., Jr. *Chem. Rev.* **1995**, *95*, 735−758.
(5) Lü, X.; Mou, X.; Wu, J.; Zhang, D.; Zhang, L.; Huang, F.; Xu, F.; Huang, S. *Adv. Funct. Mater.* **2010**, *20*, 509−515.
(6) Ding, S.; Wang, Y.; Hong, Z.; Lü, X.; Wan, D.; Huang, F. *Chem.—Eur. J.* **2011**, *17*, 11535−11541.
(7) Pan, J.; Liu, G.; Lu, G. Q.; Cheng, H.-M. *Angew. Chem., Int. Ed.* **2011**, *50*, 2133−2137.
(8) Asahi, R.; Morikawa, T.; Ohwaki, T.; Aoki, K.; Taga, Y. *Science* **2001**, *293*, 269−271.
(9) Lü, X.; Huang, F.; Mou, X.; Wang, Y.; Xu, F. *Adv. Mater.* **2010**, *22*, 3719−3722.
(10) Liu, G.; Yang, H. G.; Wang, X.; Cheng, L.; Lu, H.; Wang, L.; Lu, G. Q.; Cheng, H.-M. *J. Phys. Chem. C* **2009**, *113*, 21784−21788.
(11) Zuo, F.; Bozhilov, K.; Dillon, R. J.; Wang, L.; Smith, P.; Zhao, X.; Bardeen, C.; Feng, P. *Angew. Chem., Int. Ed.* **2012**, *51*, 6223−6.
(12) Umebayashi, T.; Yamaki, T.; Itoh, H.; Asai, K. *Appl. Phys. Lett.* **2002**, *81*, 454.
(13) Jia, L.; Wu, C.; Li, Y.; Han, S.; Li, Z.; Chi, B.; Pu, J.; Jian, L. *Appl. Phys. Lett.* **2011**, *98*, 211903.
(14) Chen, X.; Burda, C. *J. Am. Chem. Soc.* **2008**, *130*, 5018−5019.
(15) Ohno, T.; Tsubota, T.; Toyofuku, M.; Inaba, R. *Catal. Lett.* **2004**, *98*, 255.
(16) Wang, Y.; Zhang, L.; Deng, K.; Chen, X.; Zou, Z. *J. Phys. Chem. C* **2007**, *111*, 2709−2714.
(17) Liu, G.; Yan, X.; Chen, Z.; Wang, X.; Wang, L.; Lu, G. Q.; Cheng, H.-M. *J. Phys. Chem. C* **2009**, *19*, 6590.
(18) Yang, K.; Dai, Y.; Huang, B. *J. Phys. Chem. C* **2007**, *111*, 18985−18994.
(19) Chen, X.; Liu, L.; Yu, P. Y.; Mao, S. S. *Science* **2011**, *331*, 746−750.
(20) Wang, Z.; Yang, C.; Lin, T.; Yin, H.; Chen, P.; Wan, D.; Xu, F.; Huang, F.; Lin, J.; Xie, X.; Jiang, M. *Energy Environ. Sci.* **2013**, *6*, 3007−3014.
(21) Wang, Z.; Yang, C.; Lin, T.; Yin, H.; Chen, P.; Wan, D.; Xu, F.; Huang, F.; Lin, J.; Xie, X.; Jiang, M. *Adv. Funct. Mater.* [Online early access]. DOI: 10.1002/adfm.201300486, **2013**; http://onlinelibrary.wiley.com/doi/10.1002/adfm.201300486/abstract.
(22) Teleki, A.; Pratsinis, S. E. *Phys. Chem. Chem. Phys.* **2009**, *11*, 3742−3747.
(23) Wan, D.; Yang, C.; Lin, T.; Tang, Y.; Zhou, M.; Zhong, Y.; Huang, F.; Lin, J. *ACS Nano* **2012**, *6*, 9068.
(24) Grey, I. E.; Li, C.; MacRae, C. M.; Bursill, L. A. *J. Solid State Chem.* **1996**, *127*, 240−247.
(25) Pore, V.; Ritala, M.; Leskelä, M.; Areva, S.; Järn, M.; Järnström, J. *J. Mater. Chem.* **2007**, *17*, 1361.
(26) Liu, Y.; Wang, H.; Li, H.; Zhao, W.; Liang, C.; Huang, H.; Deng, Y.; Shen, H. *J. Colloid Interface Sci.* **2011**, *363*, 504−510.
(27) Grundmann, M. *The Physics of Semiconductors*; Springer-Verlag: Berlin, Heidelberg, 2010; Vol. *19*, pp 511−515.
(28) Umebayashi, T.; Yamaki, T.; Yamamoto, S.; Miyashita, A.; Tanaka, S.; Sumita, T.; Asai, K. *J. Appl. Phys.* **2003**, *93*, 5156.
(29) Tang, X.; Li, D. *J. Phys. Chem. C* **2008**, *112*, 5405−5409.
(30) Prokes, S. M.; Gole, J. L.; Chen, X.; Burda, C.; Carlos, W. E. *Adv. Funct. Mater.* **2005**, *15*, 161−167.
(31) Yu, J. C.; Yu, Y.; Ho, W.; Jiang, Z.; Zhang, L. *Chem. Mater.* **2002**, *14*, 3808−3816.
(32) Xiang, Q.; Lv, K.; Yu, J. *Appl. Catal. B: Environ.* **2010**, *96*, 557−564.
(33) Ni, M.; Leung, M. K. H.; Leung, D. Y. C.; Sumathy, K. *Renewable Sustainable Energy Rev.* **2007**, *11*, 401−425.
(34) Wang, G.; Wang, H.; Ling, Y.; Tang, Y.; Yang, X.; Fitzmorris, R. C.; Wang, C.; Zhang, J. Z.; Li, Y. *Nano Lett.* **2011**, *11*, 3026−33.
(35) Cho, I. S.; Chen, Z.; Forman, A. J.; Kim, D. R.; Rao, P. M.; Jaramillo, T. F.; Zheng, X. *Nano Lett.* **2011**, *11*, 4978−4984.
(36) Walter, M. G.; Warren, E. L.; McKone, J. R.; Boettcher, S. W.; Mi, Q.; Santori, E. A.; Lewis, N. S. *Chem. Rev.* **2010**, *110*, 6446−6473.
(37) Surendranath, Y.; Kanan, M. W.; Nocera, D. G. *J. Am. Chem. Soc.* **2010**, *132*, 16501−16509.
(38) Bediako, D. K.; Surendranath, Y.; Nocera, D. G. *J. Am. Chem. Soc.* **2013**, *135*, 3662−3674.